JOURNAL OF APPLIED ELECTROCHEMISTRY 25 (1995) 384–403

Mass transfer and electrocrystallization analyses of nanocrystalline nickel production by pulse plating

R. T. C. CHOO, J. M. TOGURI, A. M. EL-SHERIK*, U. ERB*

Department of Metallurgy and Materials Science, University of Toronto, Toronto, Ontario M5S 1A4, Canada

Received 28 December 1993; revised 10 May 1994

A comparison between the experimental process parameters employed for the pulse plating of nanocrystalline nickel and the solution-side mass transfer and electrokinetic characteristics has been carried out. It was found that the experimental process parameters (on-time, off-time and cathodic pulse current density) for cathodic rectangular pulses are consistent and within the physical constraints (limiting pulse current density, transition time, capacitance effects and integrity of the waveform) predicted from theory with the adopted postulates. This theoretical analysis also provides a means of predicting the behaviour of the process subject to a change in the system, kinetic and process parameters. The product constraints (current distribution, nucleation rate and grain size), defined as the experimental conditions under which nanocrystalline grains are produced, were inferred from electrocrystallization theory. High negative overpotential, high adion population and low adion surface mobility are prerequisites for massive nucleation rates and reduced grain growth; conditions ideal for nanograin production. Pulse plating can satisfy the former two requirements but published calculations show that surface mobility is not rate-limiting under high negative overpotentials for nickel. Inhibitors are required to reduce surface mobility and this is consistent with experimental findings. Sensitivity analysis on the conditions which reduce the total overpotential (thereby providing more energy for the formation of new nucleation sites) are also carried out. The following lists the effect on the overpotential in decreasing order: cathodic duty cycle, charge transfer coefficient, Nernst diffusion thickness, diffusion coefficient, kinetic parameter (γ) and exchange current density.

Nomenclature

A	constant employed in Fig. 8, $(\alpha nFi_0)/(RT_eC_a)$ (s^{-1})
B	constant in Equation 38 (V^2)
C	cation concentration (mol cm^{-3})
C_a	capacitance of double layer ($\mu F\,cm^{-2}$)
C_s	cation surface concentration (mol cm^{-3})
C_s^*	dimensionless cation surface concentration, C_s/C_∞ (–)
C_∞	cation bulk concentration (mol cm^{-3})
D	diffusion coefficient of cation ($cm^2\,s^{-1}$)
ΔE	total applied potential (V)
ΔE^0	standard cell potential (V)
F	Faraday constant (C mol^{-1})
$\mathscr{F}$	function defined in Appendix C (–)
Fr	frequency of waveform (Hz)
$f_{i,p}$	function defined in Appendix C for pth period (–)
$f_{i,\infty}$	function defined in Appendix C for $p \to \infty$ period (–)
G_j	function defined in Appendix B (–)
g_i	function defined in Appendix B (–)
i	current density (A cm^{-2})
i_{ac}	unsteady fluctuating a.c. current density (A cm^{-2})
i_C	capacitance current density (A cm^{-2})
i_{dc}	steady time-averaged d.c. current density (A cm^{-2})
i_F	Faradaic current density (A cm^{-2})
i_{lim}	limiting d.c. current density (A cm^{-2})
i_0	exchange current density (A cm^{-2})
i_{PL}	limiting pulse current density, $i_1\{C_s = 0$ at $t = (p-1)T + t_1\}$ (A cm^{-2})
i_1	cathodic pulse current density (A cm^{-2})
i_2	relaxed or low current pulse current density (A cm^{-2})
i_3	anodic pulse current density (A cm^{-2})
i^*	dimensionless current density, $i/\lvert i_{lim}\rvert$ (–)
i_0^*	dimensionless exchange current density, $i_0/\lvert i_{lim}\rvert$ (–)
i_{dc}^*	dimensionless steady time-averaged d.c. current density, $i_{dc}/\lvert i_{lim}\rvert$ (–)
i_{PL}^*	dimensionless limiting cathodic pulse current density, $i_{PL}/\lvert i_{lim}\rvert$ (–)
$i_{PL,p}^*$	dimensionless limiting pulse current density at pth period, $i_1(C_s = 0)/\lvert i_{lim}\rvert$ (–)
$i_{PL,\infty}^*$	dimensionless limiting pulse current density for $p \to \infty$, $i_1(C_s = 0)/\lvert i_{lim}\rvert$ (–)
i_1^*	dimensionless cathodic pulse current density, $i_1/\lvert i_{lim}\rvert$ (–)

* Department of Materials and Metallurgical Engineering, Queen's University, Kingston, Ontario K7L 3N6, Canada.

0021-891X

i_2^* dimensionless relaxed or low current pulse current density, $i_2/|i_{lim}|$ (–)
i_3^* dimensionless anodic pulse current density, $i_3/|i_{lim}|$ (–)
k electrolyte electrical conductivity ($\Omega^{-1}\,cm^{-1}$)
L characteristic length (cm)
l distance between working electrode and reference probe (cm)
m integer index and counter for eigenvalue (–)
N nucleation rate (number of nuclei $cm^{-2}\,s^{-1}$)
$\bar{N}_{ac}$ time-averaged nucleation rate when a.c. is superimposed onto the electrode (number of nuclei $cm^{-2}\,s^{-1}$)
N_{dc} nucleation rate with only d.c. polarization (number of nuclei $cm^{-2}\,s^{-1}$)
N_∞ nucleation rate at infinitely large overpotentials (number of nuclei $cm^{-2}\,s^{-1}$)
n cation valency (–)
p pth period = 1, 2, 3, ... (–)
R gas constant ($J\,mol^{-1}\,K^{-1}$)
r function defined in Appendix B (–)
s function defined in Appendix B (–)
T period (s)
T_e temperature (K)
T^* dimensionless period, DT/δ^2 (–)
t time (s)
t_c charging time of the double layer (μs)
t_d discharging time of the double layer (μs)
t^* dimensionless time, t/T (–)
t_{on} on-time or cathodic pulse period (s)
t_{off} off-time (s)
t_1 cathodic pulse period (s)
t_2 relaxed or low current pulse period (s)
t_3 anodic pulse period (s)
u dummy variable in Equation 13
v velocity vector ($cm\,s^{-1}$)
y perpendicular distance from the cathode surface (cm)

Greek symbols

α anodic charge transfer coefficient (–)
β cathodic charge transfer coefficient, $1-\alpha$ (–)
γ kinetic parameter in Butler–Volmer equation (–)
Δ degree of flattening defined by eqn. (35) (–)
δ Nernst diffusion layer thickness (cm)
θ_e current efficiency (%)
θ_1 dimensionless cathodic duty cycle, t_1/T (–)
θ_2 dimensionless relaxed or low current duty cycle, t_2/T (–)
θ_3 dimensionless anodic duty cycle, t_3/T (–)
η total overpotential (V)
η_{ac} fluctuating a.c. overpotential (V)
$\bar{\eta}_{ac}$ superimposed a.c. overpotential (V)
$\sqrt{(\eta_{ac}^2)}$ root-mean square of the superimposed overpotential (V)
η_{conc} concentration overpotential (V)
η_{dc} time-averaged d.c. overpotential (V)
η_{ohm} ohmic overpotential (V)
η_s surface overpotential (V)
η^* dimensionless total overpotential, $\{nF/RT_e\}\eta$ (–)
η_{conc}^* dimensionless concentration overpotential, $\{nF/RT_e\}\eta_{conc}$ (–)
η_{dc}^* dimensionless time-averaged d.c. overpotential, $\{nF/RT_e\}\eta_{dc}$ (–)
η_{ohm}^* dimensionless ohmic overpotential, $\{nF/RT_e\}\eta_{ohm}$ (–)
η_s^* dimensionless surface overpotential, $\{nF/RT_e\}\eta_s$ (–)
λ_m eigenvalue (–)
ρ density of electrolyte ($g\,cm^{-3}$)
$(\rho l)^*$ dimensionless ohmic resistance, $\{nF/RT_e\}\rho l i_{lim}$ (–)
τ transition time (s)

Subscripts

1 cathodic pulse
2 relaxed or low current pulse
3 anodic pulse
j index for duty cycle (1 = cathodic, 2 = relaxed, 3 = anodic)

Superscripts

* dimensionless quantity
– steady time-averaged value (bars)
~ unsteady fluctuating value

Note: vector quantities in bold face

1. Introduction

Nanocrystalline materials are solids which contain large intercrystalline volume fraction (i.e. grain boundaries and triple junctions) and possess attractive physical properties [1] such as magnetic [2], corrosion [3], thermal [4] and mechanical [5, 6]. There are numerous processing techniques for synthesizing nanocrystalline materials [1]; the more popular methods being inert gas condensation, ball milling and electrodeposition. This paper is concerned with the electrochemical production method; more specifically, the pulse plating (PP) of nanocrystalline nickel.

Most of the pioneering techniques, and thus the more prevalent, nanocrystalline processing techniques, have been in the area of gas condensation [1]. However, there are several limitations to this technique which include high costs, low production rates and high product porosities (5–25%). More recently, research at Queen's University has resulted in the development of conventional direct current (d.c.) and PP electrodeposition techniques for the production of nanocrystalline Ni–P alloys [7] and nickel [8], respectively, having uniform and controllable grain sizes down to 5 nm. Nanophase materials produced by PP have several distinct advantages over those prepared by d.c. plating which include reduced porosity [9–11] and reduced internal stresses [12]. Among the advantages of PP over gas condensation

techniques are: (i) cost, as PP involves minor modification of conventional electrodeposition technologies, (ii) process control, as electroplating process parameters can be finely tuned to produce the required grain size, alloy chemistry and texture, and (iii) versatility, as PP can be readily incorporated with codeposition technology to produce novel 'composite' materials, i.e. nanocomposites.

Despite the attractiveness and the success of the electrodeposition route for synthesis, the process parameters such as on-time (t_{on} or t_1), off-time (t_{off} or t_2) and pulse current density (i_1) have been determined by exhaustive empirical approaches. This is labourious, time consuming and expensive. It is the aim of this paper to determine if mathematical analysis of the mass transfer characteristics on the solution-side can assist in reducing the number of experiments required for defining the optimum process parameters for nanocrystals production. The ultimate goal, which is far from complete, is to relate process parameters to grain size thereby allowing nanosized grains and materials to be engineered.

2. Background information

It is generally accepted that the electrodeposited morphology is affected by pulse plating process parameters [13–16]. The following mechanisms have been identified by Chène and Landolt [17] as contributing factors to grain size: (i) solution-side mass transfer [13], (ii) nucleation rate [14, 15], (iii) adsorption–desorption reactions [13, 14] and (iv) recrystallization [13]. A more comprehensive model is given by Bockris and coworkers [18–20] who classify the electrogrowth of metals on electrodes as consisting of two stages: (a) deposition, the sequence of events that each ion follows from the movement across the double layer until it becomes incorporated onto the surface crystal lattice and (b) crystallization, the cooperative process by which aggregates of deposited adions build up or grow new crystals.

From a materials processing perspective, the 'processing-structure' relationship is very important. Identifying and understanding the range of process parameters that will produce nanosized grains is vital to the success of the processing step. The basic mechanisms of electrocrystallization attributed to Bockris *et al.* [18–20] are shown schematically in Fig. 1 where the cations from the bulk solution are finally incorporated into the crystal lattice forming grains. Within the framework of the 'processing-structure' relationship for pulse electrocrystallization, Fig. 2 shows our current – and simplified – understanding of electroplating science. The ovals represent physically measurable quantities. The physical phenomena linking these quantities are also highlighted and can be reduced to fundamental mathematical relationships, in principle.

One noticeable fact is that the link between the different physical quantities gets weaker as it proceeds further down the chain. Given the process parameters (on-time, off-time and peak current density) and with some inherent assumptions, it is possible to calculate the surface concentration of the cations from transport equations. The surface concentration is then related to the overpotential by electrokinetic equations. These two branches of electrochemistry are reasonably well established. The tie between overpotential and nucleation rate is tenuous [21–23] and that between nucleation rate and grain size is far from established [24].

Although the basic principles of electrocrystallization seem to be well established, we are still far from an adequate knowledge of the processes of nucleation, cluster orientation, grain growth interaction, dendrite formation and properties of the bulk deposits [25]. In spite of these difficulties, useful progress has been made in understanding PP

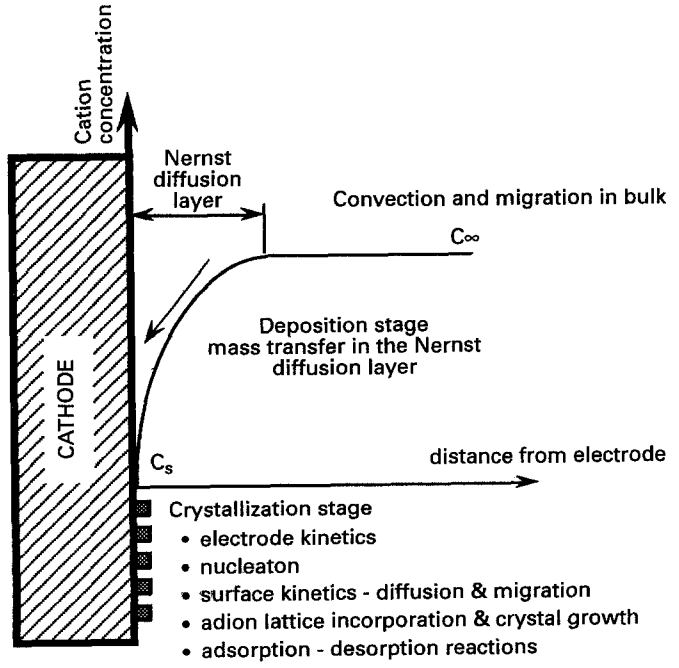

Fig. 1. Two stages of electrocrystallization according to Bockris *et al.* [18–20]. C_s is the cation surface concentration and C_∞ is the cation bulk concentration.

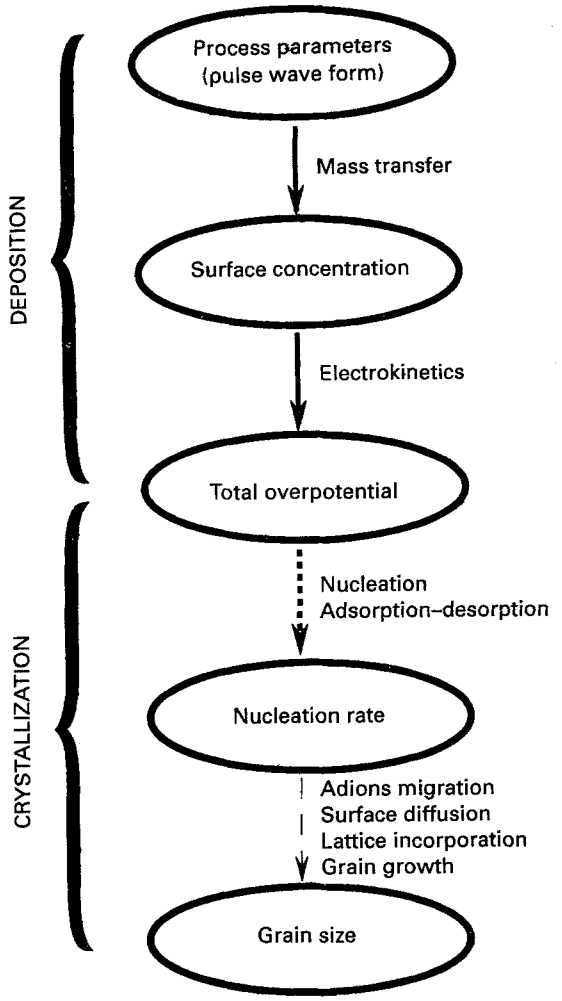

Fig. 2. 'Processing-structure' relationship for pulse electrocrystallization. Fundamental mathematical expressions describing the physical phenomena linking the physically measurable quantity (in ovals) exist as shown by the mechanisms between each oval. The links get progressively weaker down the chain and are replaced by empirical relationships towards the end.

characteristics under various process parameters [13–17, 26]. The semi-quantitative model proposed by Bockris and Razumney [20] which is based on the Kossel–Stranski model [27, 28] shall be emphasized in this paper.

The underlying hypothesis of this work is that high current densities are required for massive nucleation on the substrate [15, 29]. It follows that the massive nucleation rates should overwhelm the crystal growth rates resulting in nanosized grains. PP permits current densities which are several orders of magnitude higher than the limiting d.c. current density. It has indeed been found that finer grains are produced using PP [8, 21]. However, it has also been claimed that the finer grains are due to decreased surface mobility of adions [22]. Bockris *et al.* [19, 20] reported that the charge transfer step and the surface diffusion step are the two dominant rate-determining steps based on energy considerations. They also indicated that the charge transfer step tends to be rate limiting at high current densities [20]. Since there is evidence that the rate-determining step resides on the solution-side, the solution-side mass transfer step adopted in this work shall serve as a first step for further developmental work.

Table 1. Experimental conditions for nickel electrodeposition from Watts-type bath

Parameter	*Range*
$NiSO_4.7H_2O$	$300\,g\,dm^{-3}$
$NiCl_2.6H_2O$	$45\,g\,dm^{-3}$
Boric acid	$45\,g\,dm^{-3}$
pH	2 and 4.5
Temperature	60 and 65° C
Saccharin	0, 0.5, 2.5, 5.0 and $10.0\,g\,dm^{-3}$

From Fig. 1, the solution-side mass transfer or deposition represents the first step of the electrocrystallization process. It is also the most established and studied step relative to the other steps. In view of the objective of seeking guidelines for the successful production of nanocrystals as well as the reduction of experimental runs, this paper will focus on the solution-side mass transport and electrokinetic processes on nanocrystal production. The analyses should also help specify the physical limiting conditions for successful electrodeposition such as governed by the surface concentration or the charging times of the double layer. An overview of electrocrystallization theory as it applies to PP will also be given.

3. Experimental details

Watts-type baths (Table 1), contained in standard two-litre ($2\,dm^3$) reaction kettles, were used to produce 300 μm thick nanocrystalline and microcrystalline nickel electrodeposits [8]. Amorphous nickel electrodeposit was not produced throughout this work. Analytical grade chemicals and distilled water were used to prepare the solutions. The bath temperature was maintained at 60 or 65° C by immersing the reaction kettle in a large volume-thermostat water bath. For saccharin-containing baths, the saccharin concentration was increased from 0.5 to $10.0\,g\,dm^{-3}$. Saccharin powder was added to the plating bath which was stirred until complete dissolution was achieved prior to the commencement of plating. Electrodeposition was carried out under stagnant conditions.

A high purity (99.99%) electrolytic nickel sheet

Table 2. Plating conditions leading to electrodeposits with microcrystalline structure

On-time, t_1/ms	*Off-time,* t_2/ms	*Cathodic pulse current density,* i_1/A cm^{-2}	*Largest grain size*/μm
1	15	0.4	3
1	22	0.4	6
1	32	0.4	5
1	42	0.4	8
2.5	45	0.2	3
3	15	1.6	0.3

Table 3. Plating conditions leading to nanocrystalline structure

Saccharin /g dm^{-3}	*Temp.* /° C	*pH*	t_1 /ms	t_2 /ms	i_1 /A cm^{-2}	*Average grain size and standard deviation*/nm
0.0	60	4.5	5.0	15	1.6	110 ± 10
0.5	65	2.0	2.5	45	1.9	45 ± 5
2.5	65	2.0	2.5	45	1.9	20 ± 2
5.0	65	2.0	2.5	45	1.9	11 ± 1
10.0	65	2.0	2.5	45	1.9	11 ± 1

contained in a titanium-mesh basket was used as the soluble anode. Its surface area was approximately 10 times larger than that of the cathode to ensure that there were no problems arising from anode polarization, particularly at high current densities [30]. The cathode substrate was made of titanium sheet with an exposed surface area of 1 or 2 cm^2. The anode was placed a distance of 6 cm away from the cathode. Although quantitative measurements of the current distribution were not conducted, the large anode to cathode surface area ratio ensured a uniform current distribution. Also, the smoothness of the deposit surface and the lack of edge-growth indicated that a uniform current distribution was achieved on the cathode. The electrodeposited nickel on the titanium cathode was subsequently mechanically stripped from the substrate. Pulsed electrodeposition of nickel was carried out galvanostatically using cathodic square wave pulses with complete current cutoff.

The grain size of the microcrystalline deposits was determined by scanning electron microscopy while bright-field and dark-field transmission electron micrographs were taken for the examination of the structure of nanocrystalline deposits. Thin foils for TEM examination were prepared by electropolishing using an electrolyte comprising of 6 vol % perchloric acid, 15 vol % methanol and 79 vol % acetic acid at −10° C and 15 V d.c. The grain size of the nanocrystalline electrodeposits was determined directly from dark field transmission electron micrographs by measuring approximately 250 grains.

Table 2 shows the grain size as a function of the pulse plating parameters for electrodeposits produced from a saccharin-free Watts bath with a pH of 4.5 and a temperature of 60° C. Table 3 shows the average grain size and the calculated standard deviation for nanocrystalline deposits. As an example, Fig 3(a) and (b) show the bright-field and dark-field transmission electron micrographs, respectively, of a deposit with an average grain size of about 11 nm. Figure 3(c) shows the electron diffraction pattern of the same specimen. Figure 4 shows the grain size distribution for this deposit. It is clear from Figs 3(a)–(c) and 4 that nanocrystalline nickel electrodeposits show uniform structure with a narrow crystal size distribution. Another important feature of this structure is that some of the larger bright areas in the dark-field micrograph, Fig. 3(b), actually consist of a number of smaller grains in a similar orientation; indicating the presence of a microtexture over short distances.

4. Theoretical considerations

4.1. *Mass transfer*

The methodology proposed by Chin [31] for the analysis of the mass transfer and current–potential relationships in pulse electrolysis is adopted for this study. Figure 1 shows a schematic representation of the various processes occurring at the cathode. The cations are transferred from the bulk electrolyte to the cathode by diffusion, migration and convection. Nickel is deposited at the cathode according to the reaction:

$$Ni^{2+} + 2e^- = Ni(s) \qquad (1)$$

The following assumptions are employed:

(i) The migrational flux can be neglected due to the presence of excess supporting electrolyte. The transference number of nickel cations was calculated to be 0.02.

(ii) The physical properties of the electrolyte are assumed constant as plating is carried out under isothermal conditions in the bulk.

(iii) Buoyancy forces within the Nernst diffusion layer are neglected.

(iv) There is no homogeneous chemical reaction in the electrolyte.

(v) The charging and discharging of the double layer are neglected; the pulsating period is much greater than the charge/discharge time as will be shown later.

(vi) The analysis is for one-dimensional planar electrodes.

(vii) 100% current efficiency is assumed; otherwise the current efficiency is given by θ_e. The observed experimental current efficiency is between 96–98%.

The generalized pulse current waveform is shown in Fig. 5. All nanocrystalline samples were produced using the cathodic rectangular pulse (i_1 and t_1 are non-zero) with the relaxed or low current pulse, i_2, and the anodic pulse, i_3, both being zero. Although this waveform shall be the focus of this work, the mathematical analysis is for a generalized pulse waveform so that the mathematical relationships can be extended to anodic pulses.

The current density, at any time t, can be described as a linear combination of the steady time-averaged d.c.

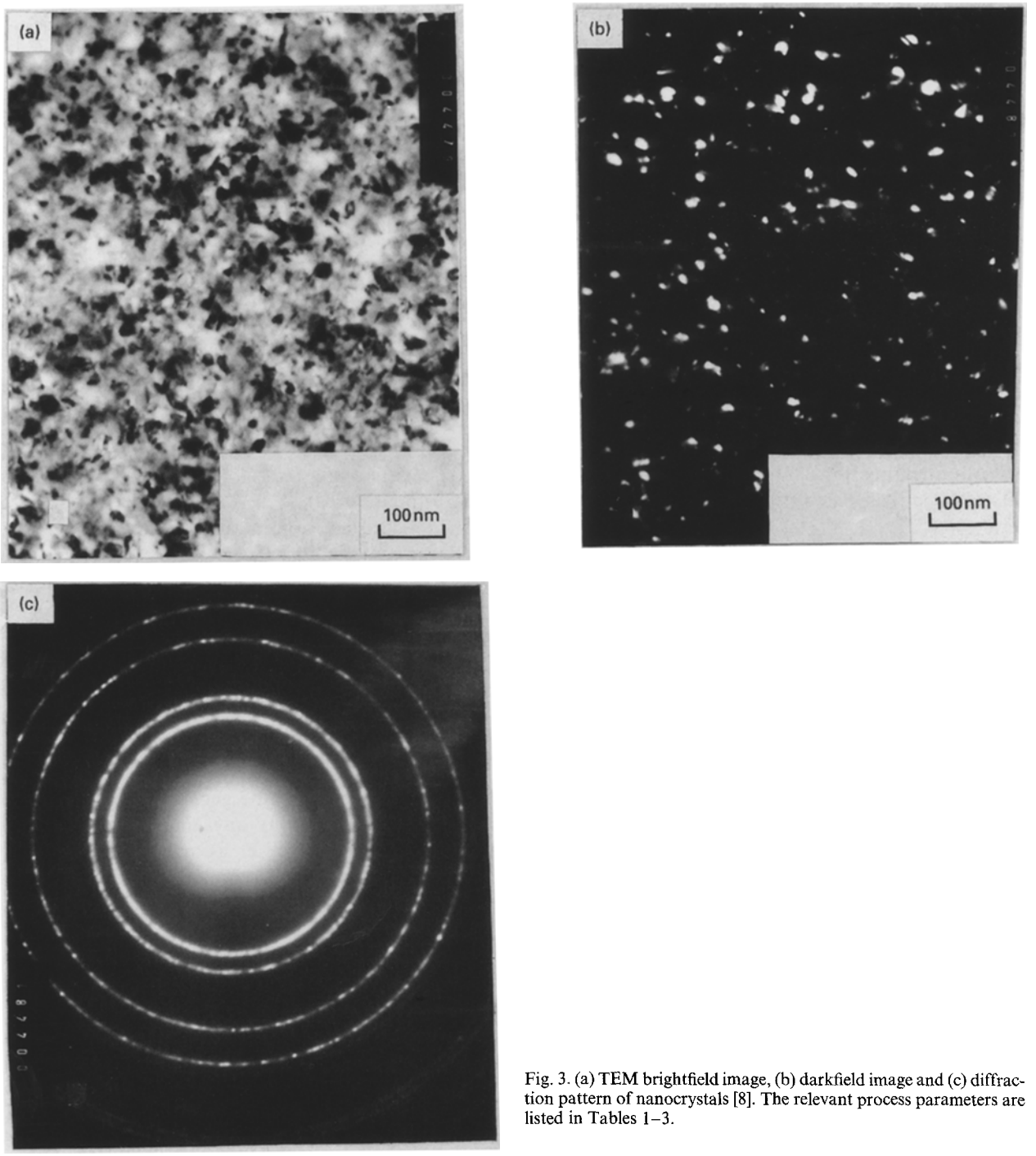

Fig. 3. (a) TEM brightfield image, (b) darkfield image and (c) diffraction pattern of nanocrystals [8]. The relevant process parameters are listed in Tables 1–3.

component and the unsteady fluctuating alternating current (a.c.) component. Thus,

$$i(t) = i_{dc} + i_{ac}(t) \tag{2}$$

where

$$i_{dc} = \frac{1}{T}(i_1 t_1 + i_3 t_2 + i_3 t_3) \tag{3}$$

With the above assumptions, the governing equation for the mass transfer of cations across the Nernst diffusion layer to the electrode surface is

$$\frac{\partial C}{\partial t} + \boldsymbol{v} \cdot \nabla C = D\nabla^2 C \tag{4}$$

together with the following boundary conditions:

$$C = C_\infty \qquad \text{at } t = 0 \text{ (initial condition)} \tag{5a}$$

$$C = C_\infty \qquad \text{at } y \to \infty \text{ (in the bulk)} \tag{5b}$$

$$-D\frac{\partial C}{\partial y} = \frac{i(t)}{nF} \qquad \text{at } y = 0 \text{ (cathode surface)} \tag{5c}^*$$

Chin [31] stated that the concentration of the diffusing species (Ni^{2+} in this case) at any time t can be written as a linear combination of the steady-state and the fluctuating components. That is,

$$C(y,t) = \bar{C}(y) + \tilde{C}(y,t) \tag{6}$$

* If current efficiency, θ_e, is not 100%, then Equation 5(c) is rewritten as $-D(\partial C/\partial y) = \theta_e i(t)/nF$.

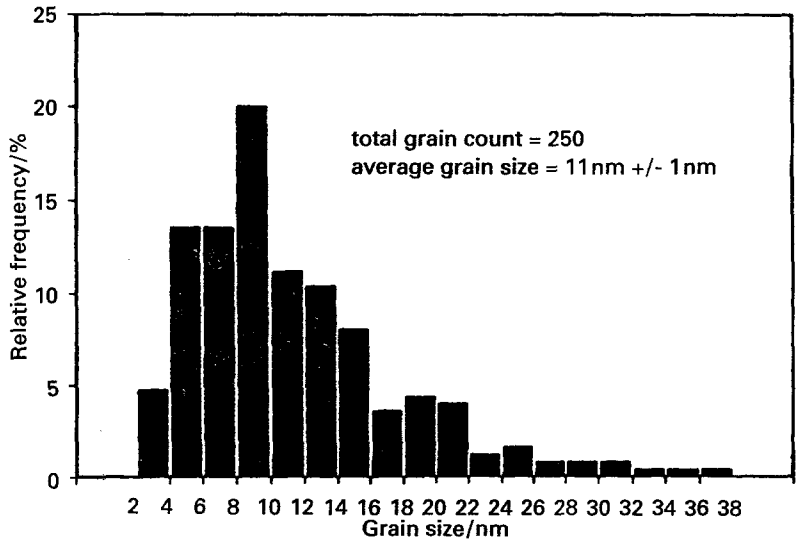

Fig. 4. Grain size distribution of nanocrystalline nickel shown in Fig. 3(b). Total grain count = 250; average grain size = 11 ± 1 nm.

Substituting Equation 6 into Equation 4 will yield two sets of equations. The first set is for the steady-state term:

$$v \cdot \nabla C = D\nabla^2 \bar{C} \tag{7}$$

together with the following boundary conditions:

$$C = C_\infty \qquad \text{at } y \geqslant \delta \text{ (Nernst diffusion layer)} \tag{8a}$$

$$-D\frac{\partial \bar{C}}{\partial y} = \frac{i_{dc}}{nF} \qquad \text{at } y = 0 \text{ (cathode surface)} \tag{8b}$$

The solution to the steady-state term in Cartesian coordinates with the convective term neglected is

$$\frac{\bar{C}_s}{C_\infty} = C_\infty - \frac{i_{dc}}{i_{lim}} \tag{9}$$

where

$$i_{lim} = -\frac{nFDC_\infty}{\delta} \tag{10}^\dagger$$

The second set is for the fluctuating component:

$$\frac{\partial \tilde{C}}{\partial t} + v \cdot \nabla \tilde{C} = D\nabla^2 \tilde{C} \tag{11}$$

together with the following boundary conditions:

$$\tilde{C} = C_\infty \qquad \text{at } t = 0 \text{ (initial condition)} \tag{12a}$$

$$\tilde{C} = C_\infty \qquad \text{at } y \to \infty \text{ (in the bulk)} \tag{12b}$$

$$-D\frac{\partial \tilde{C}}{\partial y} = \frac{i_{ac}(t)}{nF} \qquad \text{at } y = 0 \text{ (cathode surface)} \tag{12c}$$

When the Silver–Hale [32, 33] approximation is adopted, the convective term can be neglected. This omission will result in the surface concentration being 4% higher than the exact numerical solution over a wide range of conditions [31]. Under this assumption, an analytical solution can be obtained using Laplace transform. Thus,

$$\frac{\tilde{C}_s(t)}{C_\infty} = \frac{1}{nFC_\infty}\int_0^t \left(\frac{2}{\delta}\sum_{m=1}^{\infty} \exp\left[-\frac{\pi^2 D}{\delta^2}(m-\tfrac{1}{2})^2(t-u)\right]\right) \cdot (i_{ac}(u))\,du \tag{13}$$

† The rigorous definition for δ is $[C_\infty - \bar{C}_s]/[(\partial \bar{C}/\partial y)|_{y=0}]$. Chin [31] gave an incorrect definition in his paper.

The summation index m is due to the inverse Laplace transformation.

The total surface concentration at any time t is thus the linear combination of the steady-state (Equation 9) and the fluctuating components (Equation 13):

$$\frac{C_s}{C_\infty} = \frac{\bar{C} + \tilde{C}}{C_\infty} = \left(1 - \frac{i_{dc}}{i_{lim}}\right) + \frac{1}{nFC_\infty} \times \int_0^t \left(\frac{2}{\delta}\sum_{m=1}^{\infty} \exp\left[-\frac{\pi^2 D}{\delta^2}(m-\tfrac{1}{2})^2(t-u)\right]\right) \times (i_{ac}(u))\,du \tag{14}$$

Equation 14 represents the general solution for the surface concentration at any time t due to one-dimensional mass transfer (Cartesian coordinate) under the influence of a pulse current waveform as described by i_{dc} and i_{ac}. Equation 14 can be further simplified.

For the pulse current waveform given in Fig. 5, Equation 14 can be analytically integrated. The resulting dimensionless surface concentration during any period ($p = 1, 2, \ldots$) and for any duty cycle can be expressed as (see Appendix A for definition of dimensionless variables and Appendix B for definition of functions g_i, G_j, s and r):

$$C_s^* = C_s/C_\infty = 1 + i_1^*\{\theta_1(1 - G_j) + g_1\} + i_2^*\{\theta_2(1 - G_j) + g_2\} + i_3^*\{\theta_3(1 - G_j) + g_3\} + \{i_j^* - i_{dc}^*\}\{s - r\} \tag{15}$$

where $j = 1$ for cathodic duty cycle ($0 < t' < \theta_1$), $j = 2$ for low current or relaxed duty cycle ($0 < t' < \theta_2$) and $j = 3$ for anodic duty cycle ($0 < t' < \theta_3$).

Equation 15 together with Appendix B summarize the dimensionless surface concentration for any duty cycle at any period due to pulse electrolysis as predicted from the diffusion equation. The form of these equations (Appendix B) differ from those quoted by Chin [31] in that they have been simplified so that the summations are conditionally stable. Attention is drawn to the summation terms with positive indices in the exponent in Chin's paper [31] which

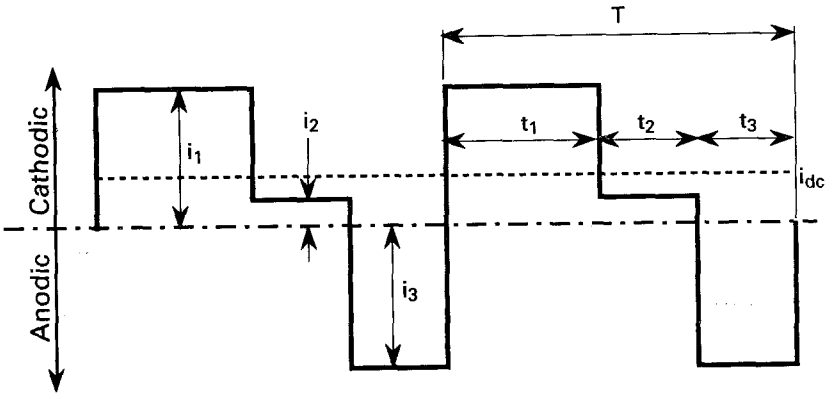

Fig. 5. Generalized pulse current waveform. The bulk of the nanocrystals in this paper was produced by the cathodic rectangular pulse ($i_2 = i_3 = t_3 = 0$). i_{dc} is the average current density and T is the period of the waveform.

sometimes lead to floating point overflows during computation. In this paper, all exponents have negative indices which are conditionally stable as $m \to \infty$.

The surface concentration (Equation 15) for infinite times ($p \to \infty$) can be determined numerically on a computer. The computed values were first compared with those reported by Chin [31] and exact agreement for the three published waveforms (cathodic rectangular, double rectangular and periodical pulse reverse) were obtained; thus providing confidence to our analyses. Using the system parameters given by Chin [31] as tabulated in Table 4, the surface concentrations for a cathodic rectangular pulse at three different cathodic current densities, i_1^*, are shown in Fig. 6(a) for the cathodic duty cycle $\theta_1 = 0.4$. First, these three curves are identical to those reported by Chin [31]. Secondly, as the cathodic current density increases, the surface concentration falls at a faster rate such that for the dimensionless peak current density of $i_1^* = -1.96$, the surface concentration drops to zero at the end of the duty cycle at $\theta_1 = 0.4$ (assigned). This i_1^* value is defined as the dimensionless limiting pulse current density, i_{PL}^* and can be much larger than the limiting d.c. current density, i_{lim}.

4.2. *Electrode kinetics*

The total applied potential consists of the standard cell potential and the total overpotential, i.e.

$$\Delta E = \Delta E^0 + \eta \tag{16}$$

where ΔE^0 and η are governed by thermodynamic and kinetic factors, respectively. Furthermore, the total overpotential consists of three components (since the charging and discharging of the double layer are neglected), i.e.

$$\eta(t) = \eta_s(t) + \eta_{conc}(t) + \eta_{ohm}(t) \tag{17}$$

For the electrochemical reaction given in Equation 1, the surface overpotential, η_s, is related to the current density by the Butler–Volmer-type equation:

$$i(t) = i_0\left(\frac{C_s(t)}{C_\infty}\right)^\gamma \times \left\{\exp\left[\frac{\alpha nF}{RT_e}\eta_s(t)\right] - \exp\left[-\frac{\beta nF}{RT_e}\eta_s(t)\right]\right\} \tag{18}$$

The concentration overpotential, η_{conc}, is due to the difference in cation concentration at the electrode surface and the bulk solution, i.e.

$$\eta_{conc}(t) = \frac{RT_e}{nF}\ln\frac{C_s(t)}{C_\infty} \tag{19}$$

The ohmic potential, η_{ohm}, is due to the electrical resistivity of the electrolyte, i.e.

$$\eta_{ohm}(t) = \rho l i(t) \tag{20}$$

In PP, the total overpotential fluctuates with time as shown by Equations 17–20. This total overpotential variation can be considered to have a form similar to Equations 6 [31]. In other words,

$$\eta(t) = \eta_{dc} + \tilde{\eta}(t) \tag{21}$$

where there is a time-averaged d.c. component and a fluctuating a.c. component. The total d.c. overpotential is then obtained by time-averaging over the whole pth period, i.e.

$$\eta_{dc} = \frac{1}{T}\int_{(p-1)T}^{pT}\eta(t)\,dt \tag{22}$$

Using the dimensionless variables defined in Appendix A, the relationship between the mass transfer and electrokinetic phenomena can then be summarized (in dimensionless form) as follows:

dim. total d.c. overpotential

$$\eta_{dc}^* = \frac{1}{T}\int_{(p-1)T}^{pT}\eta^*(t)\,dt \tag{23}$$

Table 4. Input data for Fig. 6(a) and (b) as reported from Chin [31]

Variable	*Value*
Cathodic duty cycle, θ_1	0.4
Anodic duty cycle, θ_2	0.6
Exchange current density, i_0	1.5×10^{-3} A cm^{-2}
Anodic charge transfer coefficient, α	0.75
Cathodic charge transfer coefficient, β	0.25
Kinetic parameter, γ	0.75
Diffusivity of Cu^{2+} ion, D	7.6×10^{-6} cm^2 s^{-1}
D.c. limiting current density, i_{lim}	-27.95×10^{-3} A cm^{-1}
Thickness of boundary layer, δ	2.624×10^{-3} cm*
Temperature, T_e	298 K

* There was a typographical error in Chin [31] for this value which was incorrectly quoted at 2.924×10^{-3} cm.

dim. total overpotential

$$\eta^*(t) = \eta_s^*(t) + \eta_{conc}^*(t) + \eta_{ohm}^*(t) \quad (24)$$

dim. surface overpotential

$$i^*(t) = i_0^*(C_s^*(t))^\gamma\{\exp[\alpha\eta_s^*(t)] - \exp[-\beta\eta_s^*(t)]\} \quad (25)$$

dim. concentration overpotential

$$\eta_{conc}^*(t) = \ln C_s^*(t) \quad (26)$$

dim. ohmic overpotential

$$\eta_{ohm}^*(t) = (\rho l)^* i^*(t) \quad (27)$$

To calculate the dimensionless total overpotential (Equation 24), the dimensionless surface concentration is needed. The latter can be obtained from Equation 15. The total overpotential as a function of time is then determined numerically via Equations 17–20 or via Equations 24–27 in dimensionless form. For direct comparison of this model with that of Chin [31], the ohmic potential is compensated by letting it equal to zero. Using the input data given in Table 4 and with the three cathodic current densities shown in Fig. 6(a), the respective dimensionless total overpotential are shown in Fig. 6(b). This graph is identical to that reported by Chin [31].

Both Fig. 6(a) and (b) provide quantitative and visual confidence to our model development. It is further noted that the present model has also been tested and verified for the periodic pulse reverse and the double rectangular waves used by Chin [31].

5. Results and discussion

Although the range of possible parameters for pulse plating is quite large, it is not unlimited. At one end of the spectrum, extremely large periods and on-times approach conditions similar to d.c. plating. At the other end, extremely short periods and on-times will result in unacceptable production efficiencies due to the charging and discharging of the double layer. In the same manner, the maximum applied cathodic pulse current density is limited by the surface concentration as seen in Fig. 6(a). For the production of nanocrystals, high nucleation rates are desirable. Since high overpotential associated with high pulse current density can greatly influence the nucleation rate as more energy is available for the formation of new nuclei [10], this paper shall focus on the limiting conditions specific to nanocrystal

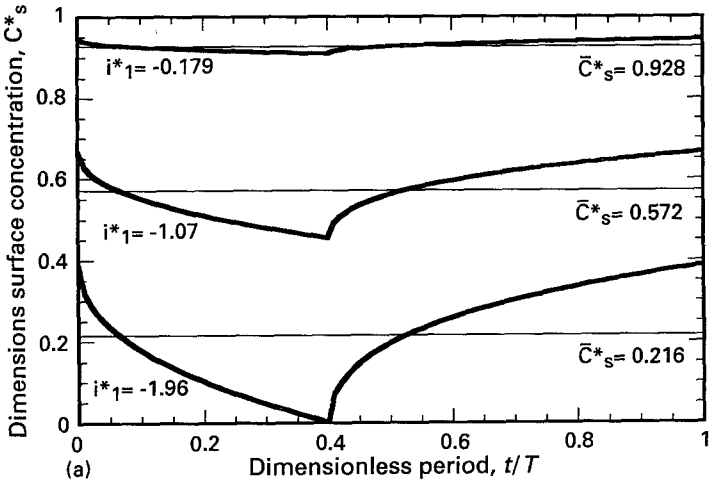

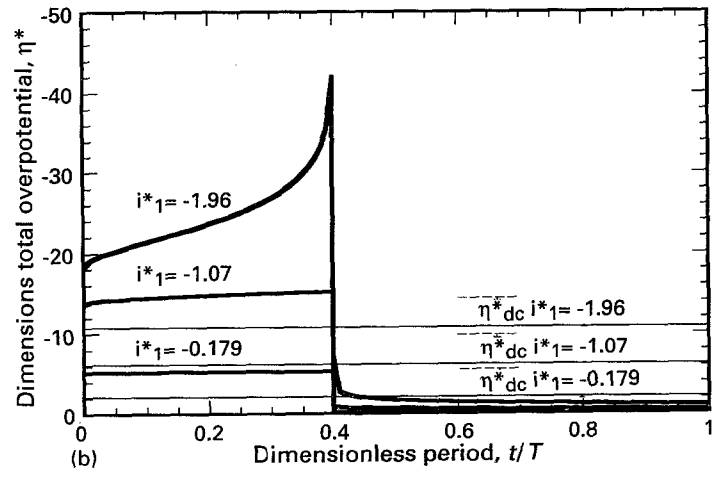

Fig. 6. Calculated (a) dimensionless surface concentration, C_s^* and (b) dimensionless total overpotential, η^*. The curves are calculated using the input data given in Table 4 which is due to Chin [31]. In (a), the parameters on the left ($i_1^* = i_1/|i_{lim}|$) are the dimensionless cathodic current density which are for the bold lines to indicate instantaneous dimensionless surface concentrations while those on the right are for the lighter lines to indicate average values. In (b), the parameters (i_1^*) on the left are for the bold lines to indicate instantaneous values while those on the right ($\overline{\eta_{dc}^*}$) are for the lighter lines to indicate average values.

production; that is, high cathodic pulse currents and short cathodic duty cycles.

Ibl [10] noted that there are three factors which limit the useful range of pulse plating conditions. These are the quality of the waveform produced by the pulse generator, the mass transfer characteristic of the deposited cation and the capacitance effect of the double layer. Commercially available pulse generators at that time (1980) have the shortest period of about 50 μs and the highest current pulse of about 2000 A. A more recent description of pulse generators has been given by Osero [34]. Only the mass transfer and capacitance effects, which are defined as 'physical constraints', will be dealt with in this paper.

There is a second class of constraint which is defined as 'product constraints'. In this instance, the goal is not so much to produce high quality deposits (smooth, non-dendritic and uniform grain size) – although they are equally important – as it is to produce grains which can be classified as nanocrystalline. While the physical constraints limit the range of feasible process parameters, the product constraints or product requirements ultimately govern the process parameters to be employed. Thus, the product constraints are likely to be more helpful in defining process parameters. These two constraints are discussed below.

5.1. *Physical constraints*

5.1.1. Physical constraint I: mass transfer effects. The pulse limiting current density represents a physical constraint for the PP process parameters. It is defined as the current density when the surface concentration becomes zero at the end of the cathodic pulse cycle. Thus,

$$i_{PL} = i_{1\{\text{at } \bar{C}_s+\tilde{C}_s=0 \text{ and } t=(p-1)T+t_1\}} \tag{28}$$

i_{PL} can be determined from Equation 15 by setting the dimensionless surface concentration to zero at the end of the dimensionless cathodic duty cycle, $p-1+\theta_1$. That is,

$$i^*_{PL,p} = \frac{i_{1(C_s^*=0 \text{ and } t^*=p-1+\theta_1)}}{|i_{lim}|} = -\frac{1+i_2^*[(1-\mathscr{F})\theta_2+f_{2,p}]+i_3^*[(1-\mathscr{F})\theta_3+f_{3,p}]}{(1-\mathscr{F})\theta_1+f_{1,p}} \tag{29}$$

where p is the period and the functions $\mathscr{F}$ and f's are defined in Appendix C. As in the case for C_s^* in Equation 15, the functions $\mathscr{F}$ and f's are expressed in forms that are conditionally stable.

For steady-state pulsating electrolysis ($p \to \infty$), $\mathscr{F} = 1$ and Equation 29 is reduced to

$$i^*_{PL,\infty} = -\frac{1+i_2^* f_{2,\infty}+i_3^* f_{3,\infty}}{f_{1,\infty}} \tag{30}$$

For cathodic rectangular pulses, $i_2^* = i_3^* = 0$ and Equation 30 is reduced to

$$i^*_{PL,\infty} = -\frac{1}{f_{1,\infty}} = -\left(2T^* \sum_{m=1}^{\infty} \frac{1-\exp[-\lambda_m\theta_1]}{\lambda_m\{1-\exp[-\lambda_m]\}}\right)^{-1} \tag{31}$$

where $T^* = DT/\delta^2$ and $\lambda_m = \pi^2 T^*(m-0.5)^2$ for $m = 1, 2, 3, \ldots, \infty$.

Equation 31 can be solved numerically. The computed values were then compared with those reported by Chin [31]. It was found that our results differ slightly when θ_1 is less than 0.1. For $\theta_1 < 0.05$ and $T^* = 0.001$, $i^*_{PL,\infty} = 14$ from this study against 18 from [31] and for $\theta_1 = 0.001$ and $T^* = 0.001$, $i^*_{PL,\infty} = 480$ from this study against 720 from [31]. This is due to the number of terms (m) or the stopping criterion used for the summation function in Equation 31. If $m = 1000$ were used, the calculated $i^*_{PL,\infty}$'s are identical to those published [31]; however, the summation function has not yet converged. Using $m = 1000$ is adequate for $0.1 < \theta_1 < 1.0$. In this study, the stopping criterion is when the subsequent term in the summation is less than 10^{-5}% of the previous term. This stopping criterion usually results in the m-index being of the order of 10^4.

Comparisons were also made with the other

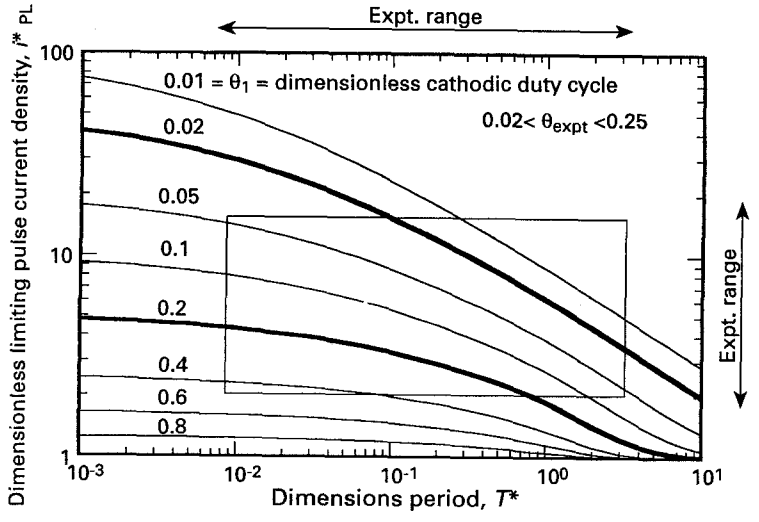

Fig. 7. Dimensionless limiting pulse current density, $i^*_{PL} = i_{1,PL}/|i_{lim}|$ against dimensionless period, $T^* = DT/\delta^2$ using the system and kinetic parameters in Table 5. The curves are for different dimensionless cathodic duty cycles, $\theta_1 = t_1/T$. The experimental range of process parameters used for depositing nanocrystals are also shown by the arrows on the top and right of the figure (boxed region). The bold lines are for θ_{expt}.

waveforms cited by Chin [31] and exact agreements were also obtained for two other waveforms (double rectangular and periodical pulse reverse) using his stopping criterion [31]; thus providing confidence to our model. Furthermore, it was found that $i_{PL,p}$ (Equation 29), or the analogous surface concentration, approaches $i_{PL,\infty}$ (Equation 30) after the 3rd or 4th period which is consistent with Rosebrugh and Miller's findings [35]. All discussion henceforth for the dimensionless limiting pulse current density refers to $i_{PL,\infty}$.

Figure 7 shows a plot of the dimensionless limiting pulse current density ($i_{PL,\infty}$) as a function of dimensionless period (T^*) using the system and kinetic parameters specific to the experimental plating conditions (Table 5). First, if $\theta_1 = 1.0$, which corresponds to d.c. plating, it is clear that $i^*_{PL} = i_{PL}/|i_{lim}| = 1.0$; that is, the limiting pulse current density is reduced to the limiting d.c. current density. Secondly, as the dimensionless cathodic duty cycle ($\theta_1 = t_1/T$) is reduced, significantly higher cathodic pulse current densities are permissible. This effect is due to the pulsating diffusion layer which is much thinner than the Nernst diffusion layer. Also, the surface concentration is replenished during the off-times. Finally, as the dimensionless period (DT/δ^2) is reduced, higher cathodic pulse current density is permissible but the increase is only significant for short dimensionless cathodic duty cycles ($\theta_1 < 0.05$).

It can also be deduced that the effect of temperature via the diffusion coefficient on i^*_{PL} is moderate. Stirring affects the thickness of the hydrodynamic boundary layer and, to some degree, the Nernst diffusion layer. However, it is known that the Nernst diffusion layer is much thinner than the hydrodynamic boundary layer [36]. Therefore, changing the cathodic duty cycle should be more effective in altering the permissible pulse current density than stirring.

The experimental process parameters that were employed for the pulse plating of nickel nanocrystals are also shown on Fig. 7 by the boxed region. The cathodic duty cycle is between 0.05 to 0.5. The dimensionless period, T^*, can be calculated using the data in Table 5 and is found to be between 0.008 to 3. Under these conditions, theory predicts that i^*_{PL} can vary between 1 to about 15. This finding is in good agreement with that actually employed (arrow on right side of Fig 7).

Despite the assumption of a 100% efficiency (the experimentally observed current efficiency is between 96–98%) and the ability to calculate the limiting current density using the simpler semi-empirical formula proposed by Ibl [10], the advantage of the present analysis is that the calculations can be extended to other pulse waveforms which include any combinations of both cathodic, relaxed and anodic pulses. These combinations can extend the range of the process parameters for nanocrystalline deposition which is currently being examined.

5.1.2. Physical constraint II: transition time. The transition time, τ, is the time required for the surface concentration to vanish to zero for a specific pulse waveform, Nernst diffusion thickness and diffusion coefficient at the end of each cathodic duty cycle. For a cathodic rectangular pulse, this value can be determined from Fig. 7 via the dimensionless period, T^*.

Landolt [36] has provided a semiempirical estimate of the transition time, τ, for rectangular cathodic pulse waveforms as

$$i^*_1 = \frac{i_1}{|i_{lim}|} = \frac{1}{\left(\frac{4}{\pi}\frac{D\tau}{\delta^2}\right)^{0.5}(1-\theta_1)^{1.5} + \theta_1} \tag{32}$$

For the present system (Table 5), using the lower limits of the process parameters ($i^*_1 = 2.5$ and $\theta_1 = 0.2$), the semiempirical model predicts the transitional times to be about 0.15 s while the more rigorous model (Fig. 7) gives 0.18 s. For the upper limit ($i^*_1 = 15$ and $\theta_1 = 0.05$), the semiempirical model

Table 5. System, kinetic and process parameters for the present study

Type of parameter	*Parameter*	*Value*
System	diffusivity of Ni^{2+} ion, D	6×10^{-6} cm^2 s^{-1}
	valency, n	2
	d.c. limiting current density, i_{lim}	(-0.2 A cm^{-2})
	thickness of boundary layer, δ	{3.79×10^{-3} cm}
	capacitance, C_a	50 μF cm^{-2}
	temperature, T_e	338 K
Kinetic	exchange current density, i_0	{5×10^{-3} A cm^{-2}}
	anodic charge transfer coefficient, α	0.5
	cathodic charge transfer coefficient, β	0.5
	kinetic parameter, γ	0.5
Process	on-times, t_1 or t_{on}	1–50 ms
	off-times, t_2 or t_{off}	19–99 ms
	period, T	20–100 ms
	cathodic pulse current density, i_1	0.5 to 3 A cm^{-2}

Note: From a review of the kinetic parameters in the literature [39, 50, 51, 53, 54], the above kinetic parameters are adopted which are representative of the present study. Data in parenthesis is measured while those in brackets are derived.

gives 0.61 ms compared with 0.75 ms for the rigorous model. Good agreements exist between the two models. However, the advantage of the rigorous model is that it can be extended to other waveforms which include anodic pulses. These represent the maximum on-times before poor deposits result when the cation surface concentration approaches zero at the end of the cathodic duty cycle [31, 36].

5.1.3. Physical constraint III: capacitance effect. The charging and discharging of the double layer represent another physical limitation. This is commonly described as capacitance effects since the electric double layer can be said to resemble a capacitor-resistance circuit [10]. In PP, part of the applied current is used to charge the double layer during the cathodic duty cycle and part of it is used to discharge the double layer during the relaxed or anodic duty cycle.

In this paper the charging and discharging of the double layer have been omitted. This assumption is valid if the pulse period is much longer than the charging/discharging times which are of the order of microseconds [10, 31]. Otherwise, there will be an extra term on the right hand side of the Butler–Volmer equation (Equation 18) due to the capacitance current as given by $\partial(C_a\eta_s)/\partial t$. A good discussion of the fundamental treatment of this extra term was given by Chin and coworkers [37, 38].

A simple yet still fundamental treatment of the capacitance effects has been given by Puippe and Ibl [39, 40]. Using their methodology, Fig. 8 shows the charging and discharge times as a function of the dimensionless pulse current density, i_1/i_0. The left vertical axis represents the charging time while the right vertical axis is for the discharging time. The vertical axes are plotted as a function of $\ln(At_c)$ and $\ln(At_d)$ where A is defined by $(\alpha nFi_0/RT_eC_a)$. For the experimental range of pulse current density that was employed in this study (shown by arrow on the top of Fig. 8 and given in Table 5) and assuming the capacitance to be $50\,\mu F\,cm^{-2}$, the charge time is between 0.02 to $0.1\,\mu s$ while the discharge time is between 0.2 to $0.7\,\mu s$. The actual experimental on and off-times are much higher (of the order of milliseconds) and so capacitance effects are not important in this study.

As a first approximation, the linear domain of Fig. 8 can be estimated as

$$t_c = 17/i_1 \tag{33}$$

$$t_d = 120/i_1 \tag{34}$$

where t_c and t_d are charging and discharging times in microseconds and i_1 is the peak cathodic current density in $A\,cm^{-2}$. The capacitance of the double layer is taken at $50\,\mu F\,cm^{-2}$ [39]. Puippe [40] reports that in the absence of reliable double layer capacitance and exchange current density data, Equations 33 and 34 are reasonable first order estimates. Despite the adopted postulates, the charging/discharging times are indeed in the order of microseconds for the process parameters that were employed in this study (Table 5).

Another physical limitation that is closely related to the charge and discharge times is the degree of flattening of the waveform due to the length of the pulse; more specifically, the off-time or t_2. Puippe and Ibl [39, 40] have defined the degree of flattening as

$$\Delta = \frac{\int_{t_1}^{t_1+t_2} i_F\,dt}{i_{dc}\,t_2} = \frac{i_1 t_1 - \int_0^{t_1} i_F\,dt}{i_{dc}\,t_2} \tag{35}$$

and

$$i_1 = i_F + i_C \tag{36}$$

where the applied current is the sum of the Faradaic current (i_F) as described by the Butler–Volmer equation and the capacitance current ($i_C = C_a[\partial\eta_s/dt]$). In Equation 35, the numerator represents the amount of metal deposited during the off-time and the denominator represents the amount which would have deposited if d.c. current is to flow during the interval between the cathodic pulses.

If the waveform is completely flattened, $\Delta = 1$ since $i_F = i_{dc}$ at all times and this waveform represents d.c. plating. A waveform that is not flattened or affected by the charging and discharging of the double layer

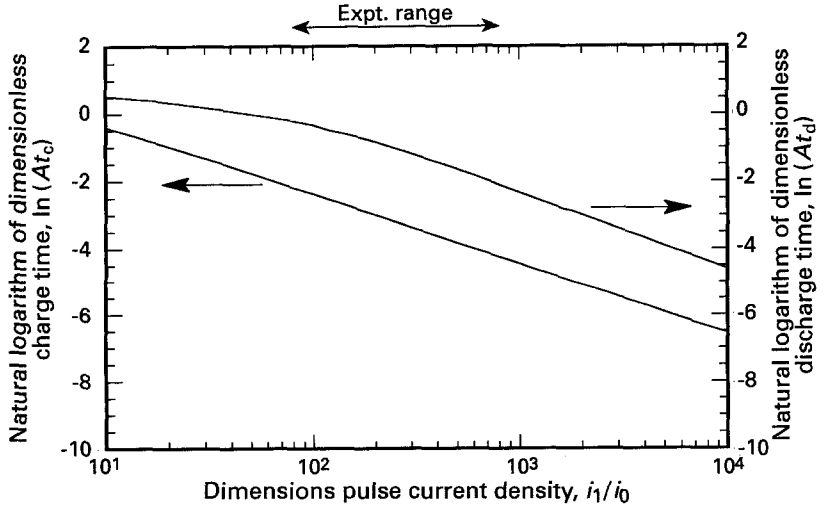

Fig. 8. Charging and discharging times of the double layer as a function of the dimensionless pulse current density (i_1/i_0) as calculated using the methodology by Puippe and Ibl [39] but with the system and kinetic parameters taken from Table 5. Constant $A = (\alpha nFi_0/RT_eC_a)$.

will have $\Delta = 0$. For pulse plating to be effective, a flattened waveform should be avoided and thus low Δ values are desirable.

Figure 9 shows the degree of flattening, Δ, as a function of on-time, t_1, as calculated from the methodology described by Puippe and Ibl [39, 40] but with the system and kinetic parameters taken from Table 5. There are three off-time to on-time ratios as indicated by the symbols (a, b and c) for the three cathodic pulse current densities, $i_1 = 10$, 1, 0.1 A cm^{-2} as shown on the top of the figure. Since the actual experimental on-times are of the order of milliseconds (Table 5) which lie to the far right of the figure, Δ is extremely small and so the pulse waveform is undamped. Thus, capacitance effects can be neglected for the process parameters that were employed in this study.

5.2. *Product constraints*

Product constraints limit the process parameters such that only nanosized grains ($\sim$ 10 to 100 nm) are to be produced. For this to be accomplished, it is important to understand the mechanisms of electrocrystallization. There is general agreement that the fundamental aspects of electrocrystallization are well established [19, 20, 25]. Budevski [25] noted that there are still further areas to be developed, particularly three-dimensional nucleation, but the basic concepts remain unchanged. The quantitative aspects of electrocrystallization are still at an early stage although the introduction of atomistic theory [25] and molecular dynamics [41] have provided significant advances. This paper focuses on the mechanisms of electrocrystallization as it applies to PP and the importance of pulsing the current for producing nanosized grains. Electrocrystallization theory has been developed primarily for d.c. plating but is also conceptually applicable to PP.

5.2.1. Qualitative description of pulse electrocrystallization. Crystallization occurs either by the build up of existing crystals or the formation and growth of new ones [42]. These two processes are in competition with each other and are influenced by different factors. Two key mechanisms have been identified as the dominant rate-determining steps: charge transfer at the electrode surface and surface diffusion of the adions on the surface crystal lattice [19, 20]. High surface diffusion rates and low overpotentials are responsible for grain growth. Conversely, low surface diffusion rates and high overpotentials enhance the creation of new nuclei. It is proposed that by having massive nucleation rates and reduced grain growth, nanosized grains are produced.

In PP, the peak current density can be considerably larger than the limiting d.c. current density. Thus, large negative overpotentials and high adion populations are expected at the electrode surface; conditions which are ideal for high nucleation rates [42]. While these two attributes are controlled by the process parameters, surface diffusion is not. Instead, surface diffusion is not only a physical attribute of its adion but is also affected by the presence of other adsorbed species on the electrode. Furthermore, extremely high nucleation rates together with excessively high adion populations may result in a situation where there is no time for atomic ordering into the crystal lattice and an amorphous structure is produced. This condition is to be avoided for this work.

A semiquantitative analysis of the mechanism leading to nucleation and grain growth has been given by Bockris *et al.* [19, 20]. This model is based on the Kossel–Stranski model [27, 28] of two-dimensional growth where the undistorted hydrated species are transferred to the electrode surface to form adions followed by surface diffusion of the adions to lattice steps, kinks or vacancies before final lattice incorporation. Another model advanced by Thirsk and Fleischmann [43] assumed the direct adion transfer to the growth site without surface diffusion. This was considered to be energetically unfavourable since their analyses did not take into account the reaction coordinate [44]. The semiquantitative treatment further showed that for a few calculated situations (Ag^+, Cu^{2+} and Ni^{2+}), the charge transfer step is rate-limiting when the potential is relatively negative

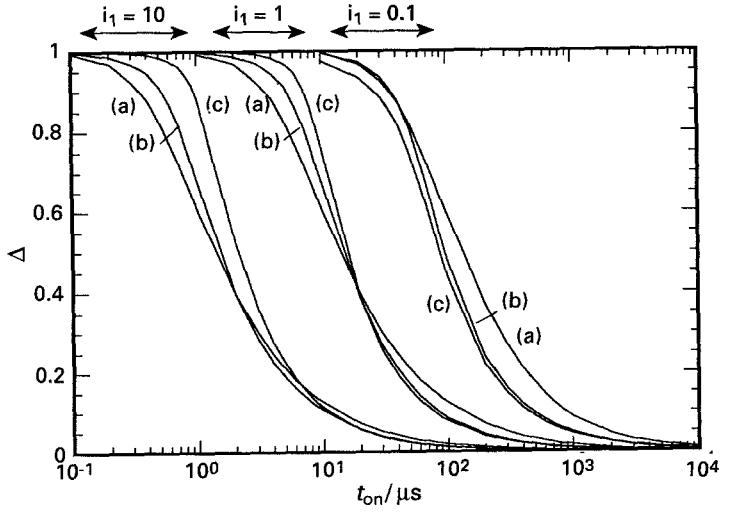

Fig. 9. Degree of flattening of the waveform (Δ) as a function of on-times (t_{on}) as calculated using the methodology by Puippe and Ibl [39] but with the system and kinetic parameters taken from Table 5. Three curves of off-time to on-time ratios: (a) $t_{off}/t_{on} = 10$; (b) $t_{off}/t_{on} = 1$; (c) $t_{off}/t_{on} = 0.1$. These are drawn for each of the three cathodic pulse current densities ($i_1 = 10$, 1 and 0.1 A cm^{-2}).

[45, 46]. The last observation is probably most critical to this work.

In PP, higher negative overpotentials can be sustained when compared with d.c. plating. This can be seen in Fig. 6(b). As the pulse current density is increased from $i_1^* = -0.179$ to -1.96, the average d.c. total overpotential is increased negatively from $\eta_{dc}^* = -2.12$ to -10.8.

Conway and Bockris [46] concluded that surface diffusion is not rate-limiting at high current densities for Ni^{2+} ion. In order to produce nanograins, it is desirable that the surface diffusion step be rate-limiting or at least be slow. In this manner, the high nucleation rates due to the high negative overpotentials in PP [10, 42] will result in massive nucleation sites while the slow surface diffusion rates will limit grain growth thereby favouring fine grains or nanograins to be produced. In reality, it is a balance between negligible surface mobility which can lead to an amorphous structure and excessive surface mobility which can lead to micrometre-sized polycrystals.

It was found that in order to produce nanograins, inhibitors were necessary and these were added to the modified Watts bath. This observation was found to be true for nickel plating where without inhibitors, micro-sized grains were obtained; probably due to excessive surface mobility and grain growth during PP when surface mobility is not rate-limiting. It is suspected that the presence of adsorbed species could interfere with the surface diffusion paths or the adions and thereby reduce diffusion rates. While the importance of inhibitors is noted, a systematic and fundamental study of the role of adsorbed species is not as straightforward. Efforts are currently being directed towards this area.

Summarizing, surface diffusion is generally rate-limiting if the overpotential is small but exceptions do exist [44]. The rate-controlling surface diffusion turns to rate-controlling charge transfer at high overpotentials in PP. Prerequisites for nanograin or fine grain production include high negative overpotential which leads to high nucleation rates and low surface mobility of adions which retards grain growth. The former is easily achieved in PP (Fig. 6(b)) but high surface mobility also results simultaneously which leads to grain growth. Thus, inhibitors are necessary to limit the surface mobility of Ag, Ni and Cu adions if nanosized grains are required. Therefore, this theory of electrocrystallization for nickel is consistent with experimental observations of nickel PP.

5.2.2. Product constraint I: current distribution (current density against overpotential). On the production line, it is desirable to maintain a uniform thickness on the electrodeposited parts. The uniformity of a deposit is related to the uniformity of the current distribution which can be described as primary, secondary or tertiary depending upon the dominant mechanisms occurring on the electrode [47]. The primary current distribution neglects polarization effects and is only a function of the geometry of the electrode. Secondary distribution includes the effect of surface or activation polarization but neglects the effect of the diffusion layer thickness on the deposited morphology. Tertiary distribution becomes dominant if both activation and mass transfer effects contribute to the polarization resistance. For PP, polarization effects are important (Fig. 6(b)) and the pulsating diffusion layer is very thin (of the order of micrometres). Thus, the secondary and tertiary current distributions must be addressed.

The secondary current distribution can be quantified via the Wagner number. That is, via

$$Wa = \frac{k}{L}\frac{\partial \eta}{\partial i_{dc}} \approx 2.3\frac{k}{L}\frac{\partial \eta}{\partial \log i_{dc}} \qquad (37)$$

which is a ratio of the activation against ohmic polarization. A semiquantitative analysis shows that a high Wa number corresponds to a more uniform current distribution and deposit thickness [47].

Figure 10 shows the dimensionless total d.c. overpotential (Equation 23) as a function of the dimensionless d.c. current density (Equation A10) and from which the Wa number can be derived. The various curves are for different dimensionless cathodic duty cycles, $\theta_1 = t_1/T$. For d.c. plating, $\theta_1 = 1$. Pulsing reduces the d.c. total overpotential for the

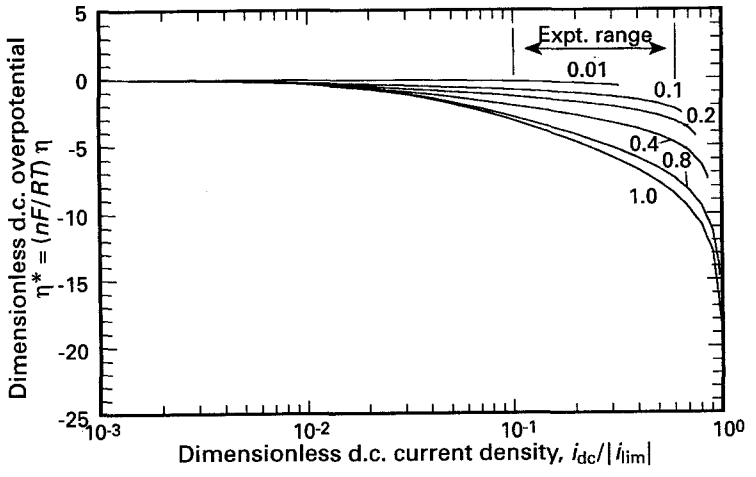

Fig. 10. Dimensionless d.c. polarization curve for pulse electrolysis with rectangular cathodic current pulses. The system and kinetic parameters are taken from Table 5 and the period is 0.1 s (10 Hz). The various curves are for different dimensionless cathodic duty cycles, $\theta_1 = t_1/T$.

nickel deposition reaction. Also, for $\theta_1 < 1$, the time-averaged d.c. current density, i_{dc}, cannot be greater than the d.c. limiting current density, $|i_{lim}|$ [31]. Although Fig. 10 is plotted in d.c. quantities, both dimensions can be related to PP quantities through constant multipliers (nF/RT_e and i_{lim}). Furthermore, since a cathodic rectangular pulse is used and the on-times are above the charging times of the double layer, the instantaneous overpotential is, for the most part, constant with respect to the instantaneous current density within each period (Fig. 6(b)). The regime where the experimental work is carried out is also shown on Fig. 10 and it is noted that the slope of the curve is rather shallow unless high $i_{dc}/|i_{lim}|$ values are used.

Both the semiquantitative [47] and the more quantitative [31] analyses showed that PP will produce a less uniform current density, and thus a less uniform deposit, when compared with d.c. plating. The slope of the d.c. polarization curves in Fig. 10 for PP ($\theta_1 < 1$) is always less than that of d.c. plating ($\theta_1 = 1$). Ossenbach [47] recommended that the current distribution in PP could be improved by having on-times shorter than the charge times such that double layer capacitance effects can come into play. This is undesirable for reasons described in Section 5.1.3.

Tertiary current distribution is obtained when the on-time is an order of magnitude larger than the transition time such that deposition takes place under mass transport controlled (limiting current) conditions [47]. The distribution is best described by the microprofile (low *Wa*) and macro-profiles (high *Wa*) of the deposit. Nanocrystal plating would be classified as a microprofile since the size of the nucleated grains (of the order of nanometres) is much less than the thickness of the pulsating diffusion layer (of the order of micrometres). This microprofile corresponds to a low *Wa* number and thus a less uniform current distribution. As the on-times are usually much less than the transition times in this paper, tertiary current distribution is not important.

The demand between a uniform deposited thickness and that of controllable nanosized grains represents opposing forces in competition. While PP will generally result in a less uniform deposit for a cathodic rectangular pulse and consequently a likely larger variation in grain size, PP is still required to produce nanograins for reasons described in the previous section (high overpotentials and nucleation rates). Ossenbach [47] suggested that pulse reverse waveforms (both anodic and cathodic pulses) be employed to tackle the problem of nonuniform deposits and there have been some successes using this technique. Chin [31] also showed that pulse reverse represents a good alternative as the *Wa* number is usually larger when compared to d.c. plating for the same average current density. Work on pulse reverse plating of nanocrystal is currently in progress.

The above analysis is based on an electrolyte without inhibitors or levelling agents. On the experimental side, levelling agents are added to ensure uniform deposits. Theoretical analysis showed that secondary currents in PP with the simple cathodic rectangular pulse waveform will result in a nonuniform deposit and probably nonuniform grain sizes. From this perspective, the role of levelling agents is again important.

5.2.3. Product constraint II: overpotential and nucleation rate. The grain size is a function of, among other factors, the nucleation rate which is related to the total overpotential [48]:

$$N = N_\infty \exp(-B/\eta^2) \tag{38}$$

where

$$\eta(t) = \eta_{dc} + \tilde{\eta}_{ac}(t) \tag{39}$$

and B is a constant which is dependent upon temperature and electrode deposition reactions. A more elaborate description of the nucleation equation (Equation 38) is given by Budevski [49] where N_∞ and B are functions of temperature, valency, geometry of the nucleating cluster and adatom, surface energy of the adatom, and frequency of attachment and detachment of atoms to and from growth sites. An important observation of the nucleation equation is that the nucleation rate only becomes significant after a critical overpotential is reached [25]. Experimental verifications of the nucleation equation have been obtained for Ag, Pb, Zn and Hg [48]. Chin and Venkatesh [49] claimed that the nucleation rate can be enhanced in PP according to the following equation:

$$\frac{\bar{N}_{ac}}{N_{dc}} = \frac{\exp\left[-\dfrac{1}{(1+\eta_{ac}/\eta_{dc})^2(\eta_{dc}/B)^2}\right]}{\exp\left[-\dfrac{1}{(\eta_{dc}/B)^2}\right]} \tag{40}$$

A plot of Equation 40 is shown in Fig. 11. The bold horizontal line is for d.c. plating when the parameter $\sqrt{(\eta_{ac}^2)}/\eta_{dc} = 0$ as there is no a.c. fluctuation in d.c. plating. $\sqrt{(\eta_{ac}^2)}$ is the root-mean square of the superimposed overpotential. As this parametric value is increased, it can be seen that for values of $(\eta_{dc}/B) < 1$, the time-averaged a.c./d.c. nucleation rate is enhanced. The total overpotential in PP can be expressed by Equation 39 from which the $\sqrt{(\eta_{ac}^2)}/\eta_{dc}$ ratio can be calculated. Typical values of this ratio for the process parameters that were employed for this work are between 0.05 and 0.15. Unfortunately, the value for B is not easily determined [49]. It can only be concluded that with the current waveforms employed, there is a potential for enhanced nucleation rate when PP is used.

5.2.4. Product constraint III: nucleation rate and grain size. Although the ultimate goal is to predict the grain size from the process parameters on the basis of first principles, this goal is far from being achieved. The most recent fundamental work on

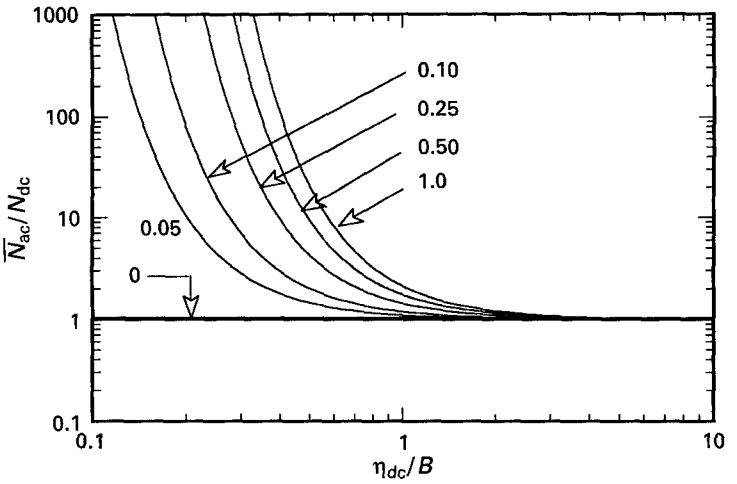

Fig. 11. Effect of cathodic rectangular pulses on the a.c./d.c. nucleation rate ratio. The parameters on the graph are for $\sqrt{(\overline{\eta_{ac}^2})}/\eta_{dc}$ ratios. D.c. plating corresponds to $\sqrt{(\overline{\eta_{ac}^2})}/\eta_{dc} = 0$ since there is no a.c. fluctuation and so $\overline{N_{ac}} = N_{dc}$.

electrocrystallization was focussed on the effects of concurrent redox reactions and of surface diffusion on surface nucleation and three-dimensional growth [24]. This paper also noted that the effects of cluster interactions and overlapping of growth centres, a prelude to grain growth, must still be addressed.

The efforts required for the determination of the fundamental relationship between grain size and nucleation rate will be a monumental one. Not only do the effects of multiple-steps charge transfer, surface diffusion and adsorbed species have to be accounted for, studies on single crystals reveal that each crystal plane grow at different speed [18]. Bockris and Reddy [18] claimed that the basic mechanisms for single crystal electrogrowth are still valid for polycrystals by considering each grain as a single crystal microsubstrate. It is probably correct to conclude that the same principles are true for nanocrystals since the ionic radius of Ni^{2+} is 0.072 nm and the grain size that is typically produced in this study is between 5 and 200 nm. It is also clear that this phase of the work requires molecular dynamics simulations [41] and is beyond the scope of this paper.

There have been some empirical studies of the correlation between grain characteristics and process parameters [13, 17]. One study [17] correlated the mean dendrite size with the pulsating diffusion layer for different deposit thickness. The pulsating diffusion layer is related to the PP process parameters.

5.3. *Factors that assist in grain refinement*

From the qualitative description of pulse electrocrystallization, it is concluded that high negative overpotential and high adion population at the electrode surface are necessary for high nucleation rate which is a prerequisite for grain refinement. While PP can easily achieve a high negative overpotential, it is also helpful to do a sensitivity analysis of the variables that affect it, more specifically, the magnitude of the change in the overpotential due to a small change of these variables.

Table 6 shows the sensitivity analysis of the various variables that would reduce the overpotential. By reducing the overpotential required for the nickel deposition reaction, more energy will be provided for the formation of new nuclei [10]. The overpotential change is calculated from the dimensionless d.c. polarization curve such as that given in Fig. 10. The reference case is for $i_1/|i_{lim}| = 0.99$ and $\theta_1 = 0.1$. The system and kinetic parameters are taken from Table 5. Each variable is changed by a factor of two to ensure a drop in the overpotential. Although this analysis does not imply a linear change of the affected variables beyond a factor of two, it does give an order of magnitude perspective of the change.

It can be seen from Table 6 that significant decreases (> 20%) in the overpotential occur when changes are made to the duty cycle and the cathodic charge transfer coefficient. Moderate decrease (10–20%) is observed when the limiting current density is doubled while the diffusion coefficient, kinetic parameter (γ) and the exchange current density do not cause significant changes ($\leqslant 10\%$) to the overpotential. The effect of the decrease in frequency on lowering the overpotential is more sensitive at lower duty cycle. By knowing the sensitivities of these trends, one can make the appropriate modifications to the kinetic, system or process parameters in order to affect the nucleation rates.

The qualitative description of pulse electrocrystallization also concluded that at high negative overpotentials, the charge transfer step is rate-limiting. The electrode kinetics is grouped empirically under the Butler–Volmer equation (Equation 18). Tabulated kinetic parameters [50, 51] showed that the charge transfer coefficients are strong functions of applied potential and solution composition. While the capacitance of the double layer is strongly affected by electrode surface preparation, this is not so for the kinetic parameters. It was found that the initial state of the titanium substrate did not affect the plating process nor the size of the nanograins produced. This observation is consistent with the proposal by Conway and Bockris [46] that the charge transfer step is rate-limiting. Thus, emphasis should be placed on the solution composition, particularly the presence of inhibitors, which can critically affect the charge transfer coefficients and thus the nucleation rate and step.

Table 6. Variables that decrease the total overpotential

Variable	*Change*	*Parameter*	*Overpotential*	*Change*
Decrease duty cycle, $\theta_1 = t_1/T$	0.2 to 0.1	$Fr = 10$ Hz	−4.176 to −2.502	[−40%]
		$Fr = 50$ Hz	−4.998 to −3.177	[−36%]
Increase cathodic transfer coefficient, β	0.25 to 0.50	$Fr = 10$ Hz	−3.912 to −2.502	[−36%]
		$Fr = 50$ Hz	−4.703 to −3.177	[−32%]
Increase limiting current density, i_{lim} (decrease diffusion layer)	0.1 to 0.2 A cm^{-2}	$Fr = 10$ Hz	−2.940 to −2.502	[−15%]
		$Fr = 50$ Hz	−3.671 to −3.177	[−13%]
Decrease diffusion coefficient, D	6×10^{-6} to 3×10^{-6} cm^2 s^{-1}	$Fr = 10$ Hz	−2.502 to −2.253	[−10%]
		$Fr = 50$ Hz	−3.177 to −2.878	[−9%]
Decrease kinetic parameter, γ	1.0 to 0.5	$Fr = 10$ Hz	−2.606 to −2.398	[−8%]
		$Fr = 50$ Hz	−3.305 to −3.048	[−8%]
Increase exchange current density, i_0	0.0025 to 0.005 A cm^{-2}	$Fr = 10$ Hz	−2.639 to −2.502	[−5%]
		$Fr = 50$ Hz	−3.314 to −3.177	[−4%]
Decrease frequency $Fr = 1/T$	20 Hz to 10 Hz	$\theta_1 = 0.01$	−0.690 to −0.565	[−18%]
		$\theta_1 = 0.1$	−2.785 to −2.502	[−10%]

Standard case: cathodic duty cycle, t_1/T is 0.1 unless stated; cathodic pulse current density, i_1, used is 99% i_{lim}.
Note: The reference case data are taken from Table 5. The variable change occurs by a factor of 2. The reference process parameters are $i_1^* = 0.00$ and $\theta_1 = 0.1$.

6. Conclusions

The experimental process parameters (on-time, off-time and cathodic pulse current density) which were employed for the pulse electrolytic production of nanocrystalline nickel using rectangular cathodic pulse waveforms were compared with the theoretically predicted results based on solution-side mass transfer and electrokinetic characteristics. The objective is to determine the physical and product constraints of the process parameters that limit nanograin production. The physical constraints are determined from mass transfer and double layer capacitance effects while the product constraints, defined as the experimental conditions under which nanocrystalline grains are produced, are inferred from electrocrystallization theory.

The following conclusions are noted:

(i) The experimental process parameters are consistent and within the physical constraints (limiting pulse current density, transition time, capacitance effects and integrity of the waveform) predicted from theory.

(ii) High negative overpotential, high adion population and low adion surface mobility are prerequisites for massive nucleation rates and reduced grain growth; conditions which are suited for nanograin production.

(iii) Pulse plating can satisfy the former two requirements but calculations by Conway and Bockris [46] showed that adion surface mobility is not rate-limiting under high negative overpotentials. Inhibitors are required to reduce surface mobility and this is consistent with the experimental findings.

(iv) Sensitivity analyses have been carried out to determine variables that will reduce (increase negatively) the dimensionless total d.c. overpotential such that the electrokinetic requirement for the deposition reaction is reduced; thereby providing more energy for the formation of new nucleation sites. Large decreases (>20%) are observed for changes (factor of 2 or 1/2) in the duty cycle and the cathodic charge transfer coefficient while moderate decrease (10–20%) is observed when the limiting current density (or conversely the thickness of the Nernst diffusion layer) is doubled. The diffusion coefficient, kinetic parameter (γ) and exchange current density do not cause significant changes ($\leqslant 10\%$) to the overpotential.

Acknowledgements

The authors wish to thank the Ontario Center for Materials Research (OCMR) for financial support of this investigation through a Seed Fund Grant. The authors are also grateful to H. W. Siu for writing the computer program for the mathematical model.

References

[1] H. Gleiter, *Prog. Mat. Sci.* **33** (1989) 223.
[2] G. Herzer, *Mat. Sci. Eng.* **A133** (1991) 1.
[3] S. J. Thorpe, B. Ramaswami and K. T. Aust, *J. Electrochem. Soc.* **135** (1988) 2162.
[4] K. Boylan, D. Ostrander, U. Erb, G. Palumbo and K. T. Aust, *Scripta Metall. Mater.* **25** (1991) 2711.
[5] R. W. Siegel and H. Hahn, 'Nanophase Materials: Current Trends in Physics of Materials' (edited by M. Youssef), World Scientific Publications, Singapore (1988).
[6] J. Karch, R. Birringer and H. Gleiter, *Nature* **330** (1987) 556.
[7] G. McMahon and U. Erb, *J. Mater. Sci. Lett.* **8** (1989) 865.
[8] A. M. El-Sherik and U. Erb, 'Production of nanocrystalline metals', *US Patent Allowed 07/983 205* (1992).
[9] M. Cherkaoui, E. Chassaing and K. Vu Quang, *Surf. Coat. Technol.* **34** (1988) 242.
[10] N. Ibl, *Surf. Technol.* **10** (1980) 81.
[11] K. I. Popov, M. D. Maksimovic, B. M. Ocokoljie and B. J. Lazarevic, *ibid.* **11** (1980) 99.
[12] K. Hosokawa, J. C. Puippe and N. Ibl, Proceedings of the World Congress on Met. Finish, 10th, Interfinish 80, Met. Soc. of Japan, Tokyo (1980) pp. 59–62.

[13] N. Ibl, J. Cl. Puippe and H. Angerer, *Surf. Technol.* **6** (1978) 287.
[14] D. T. Chin, R. Sethi and J. McBreen, *J. Electrochem. Soc.* **129** (1982) 2677.
[15] J. Cl. Puippe and N. Ibl, *Plating Surf. Finish.* **67** (1980) 68.
[16] M. G. Pavlovic, M. D. Maksimovic and K. I. Popov, *J. Appl. Electrochem.* **8** (1978) 61.
[17] O. Chène and D. Landolt, *ibid.* **19** (1989) 188.
[18] J. O'M. Bockris and A. K. N. Reddy, 'Modern Electrochemistry', vol. 2, Plenum Press, New York (1970) pp. 1173–1231.
[19] J. O'M. Bockris and A. Damjanovic, The Mechanism of the Electrodeposition of Metals, *in* 'Modern Aspects of Electrochemistry', vol. 3, (edited by J. O'M. Bockris and B. E. Conway), Butterworth, London (1964) pp. 224–346.
[20] J. O'M. Bockris and G. A. Razumney, 'Fundamental Aspects of Electrocrystallization', Plenum Press, New York (1967) pp. 27–38.
[21] D.-T. Chin and S. Venkatesh, *J. Electrochem. Soc.* **128** (1981) 1439.
[22] G. Holmbom and B. E. Jacobson, *ibid.* **135** (1988) 2720.
[23] J. O'M. Bockris and B. E. Conway (eds), *op. cit.* [19], p. 279.
[24] M. Y. Abyaneh and M. Fleischmann, *J. Electrochem. Soc.* **139** (1991) 2491.
[25] E. B. Budevski, Deposition and Dissolution of Metals and Alloys. Part A: Electrocrystallization, *in* 'Comprehensive Treatise of Electrochemistry', vol. 7, (edited by B. E. Conway, J. O'M. Bockris, E. Yeager, S. U. M. Khan and R. E. White), Plenum Press, New York (1983) pp. 399–450.
[26] W. Kim and R. Weil, *Surf. Coat. Technol.* **38** (1989) 289.
[27] W. Kossel, *Nachr. Ges. Wiss. Göttinger, Math. Physik. Kl.* (1929) 135.
[28] I. N. Stranski, *Z. Physik. Chem. Leipzig* **136** (1928) 259.
[29] D. L. Rehrig, *Plating* **61** (1974) 43.
[30] N. V. Parthasaradhy, 'Practical Electroplating Handbook', Prentice Hall, Englewood Cliffs, NJ (1989).
[31] D. T. Chin, *J. Electrochem. Soc.* **130** (1983) 1657.
[32] Yu G. Silver, *Zh. Fiz. Khim.* **34** (1960) 577.
[33] J. M. Hale, *J. Electroanal. Chem.* **6** (1963) 187.
[34] N. Osero, Pulse plating equipment, *in* 'Theory and Practice of Pulse Plating', (edited by J. Cl. Puippe and F. Leaman), AESF, Orlando, FA (1986) pp. 221–228.
[35] T. R. Rosebrugh and W. L. Miller, *J. Physical Chem.* **14** (1910) 816.
[36] D. Landolt, Mass transport in pulse plating, *in* 'Theory and Practice of Pulse Plating', (edited by J. Cl. Puippe and F. Leaman), AESF, Orlando, Florida (1986) pp. 55–71.
[37] S. Venkatesh, M. Meyyappan and D.-T. Chin, *J. Colloid & Interf. Sci.* **85** (1982) 216.
[38] S. Sethi and D.-T. Chin, *J. Electroanal. Chem.* **160** (1984) 79.
[39] J. Cl. Puippe and N. Ibl, *J. Appl. Electrochem.* **10** (1980) 775.
[40] J. Cl. Puippe, Influence of charge and discharge of double layer in pulse plating, *in* 'Theory and Practice of Pulse Plating', (edited by J. Cl. Puippe and F. Leaman), AESF, Orlando, FA (1986) pp. 41–54.
[41] C. M. Gilmore and J. A. Sprague, 'Molecular dynamics simulations of thin film nanostructures', 1993 TMS–AIME Annual General Meeting, Denver, paper in session on nanocrystalline materials.
[42] J. Cl. Puippe, Qualitative approach to pulse plating, *in* 'Theory and Practice of Pulse Plating', (edited by J. Cl. Puippe and F. Leaman), AESF, Orlando, FA (1986) pp. 1–15.
[43] M. Fleischmann and H. R. Thirsk, Metal deposition and electrocrystallization, *in* 'Advances in Electrochemistry and Electrochemical Engineering', (edited by P. Delahay and C. W. Tobias), Interscience, New York (1963) pp. 123–210.
[44] J. O'M. Bockris and G. A. Razumney, *op. cit.* [20], pp. 51–53.
[45] *Idem, op. cit.* [20], p. 38.
[46] B. E. Conway and J. O'M. Bockris, *Electrochim. Acta* **3** (1961) 340.
[47] O. Dossenbach, Current distribution in pulse plating, *in* 'Theory and Practice of Pulse Plating', (edited by J. Cl. Puippe and F. Leaman), AESF, Orlando, FA (1986) pp. 73–92.
[48] D.-T. Chin and S. Venkatesh, *J. Electrochem. Soc.* **128** (1981) 1439.
[49] E. B. Budevski, *op. cit.* [25], p. 441.
[50] A. J. Arvia and D. Posadas, Nickel, *in* 'Encyclopaedia of Electrochemistry of the Elements', vol. 3, (edited by A. J. Bard), Marcel and Dekker, New York (1975) pp. 211–421.
[51] N. Tanaka and R. Tamamushi, *Electrochim. Acta* **9** (1964) 963.
[52] J. Y. Wang, D. Balamurugan and D.-T. Chin, *J. Appl. Electrochem.* **22** (1992) 240.
[53] S.-C. Yen and T. W. Chapman, *Chem. Eng. Comm.* **38** (1985) 159.
[54] M. Datta and D. Landolt, *Electrochim. Acta* **26** (1981) 899.

Appendix A: Definition for dimensionless variables

time

$$t^* = t/T \tag{A1}$$

cathodic pulse time

$$\theta_1 = t_1/T \tag{A2}$$

relaxation pulse time

$$\theta_2 = t_2/T \tag{A3}$$

anodic pulse time

$$\theta_3 = t_3/T \tag{A4}$$

period

$$T^* = DT/\delta^2 \tag{A5}$$

surface concentration

$$C_s^* = C_s/C_\infty \tag{A6}$$

cathodic pulse current density

$$i_1^* = i_1/|i_{\text{lim}}| \tag{A7}$$

relaxed pulse current density

$$i_2^* = i_2/|i_{\text{lim}}| \tag{A8}$$

anodic pulse current density

$$i_3^* = i_3/|i_{\text{lim}}| \tag{A9}$$

d.c. current density

$$i_{\text{dc}}^* = (i_1^* t_1 + i_2^* t_2 + i_3^* t_3)/T \tag{A10}$$

pulse limiting current density

$$i_{\text{PL}}^* = i_{\text{PL}}/|i_{\text{lim}}| \tag{A11}$$

total overpotential

$$\eta^*(t) = \{nF/RT_e\}\eta(t) \tag{A12}$$

exchange current density

$$i_0^* = i_0/|i_{\text{lim}}| \tag{A13}$$

ohmic resistance

$$(\rho l)^* = \{nF/RT_e\}\rho l\,|i_{\text{lim}}| \tag{A14}$$

Appendix B: Definition of functions for Equation 15

The functions are expressed in a form so as to avoid floating point overflow during summation.

(*i*) *Cathodic duty cycle* $(0 < t^* < \theta_1)$

$$g_1 = 2T^* \sum_{m=1}^{\infty} \left\{ \frac{\{\exp[-\lambda_m(t^* + \theta_2 + \theta_3)] - \exp[-\lambda_m(t^* + \theta_2 + \theta_3 + \theta_1)]\}}{\lambda_m} \times \left\{ \frac{1 - \exp[-\lambda_m(p-1)]}{1 - \exp[-\lambda_m]} \right\} \right\} \tag{B1}$$

$$g_2 = 2T^* \sum_{m=1}^{\infty} \left\{ \frac{\{\exp[-\lambda_m(t^* + \theta_3)] - \exp[-\lambda_m(t^* + \theta_3 + \theta_2)]\}}{\lambda_m} \times \left\{ \frac{1 - \exp[-\lambda_m(p-1)]}{1 - \exp[-\lambda_m]} \right\} \right\} \tag{B2}$$

$$g_3 = 2T^* \sum_{m=1}^{\infty} \left\{ \frac{\{\exp[-\lambda_m t^*] - \exp[-\lambda_m(t^* + \theta_3)]\}}{\lambda_m} \times \left\{ \frac{1 - \exp[-\lambda_m(p-1)]}{1 - \exp[-\lambda_m]} \right\} \right\} \tag{B3}$$

$$G_1 = g_1 + g_2 + g_3 = 2T^* \sum_{m=1}^{\infty} \left\{ \frac{\{\exp[-\lambda_m t^*]}{\lambda_m} \times \{1 - \exp[-\lambda_m(p-1)]\} \right\} \tag{B4}$$

(*ii*) *Relaxed or low current duty cycle* $(0 < t^* < \theta_2)$

$$g_1 = 2T^* \sum_{m=1}^{\infty} \left\{ \frac{\{\exp[-\lambda_m t^*] - \exp[-\lambda_m(t^* + \theta_1)]\}}{\lambda_m} \times \left\{ \frac{1 - \exp[-\lambda_m p]}{1 - \exp[-\lambda_m]} \right\} \right\} \tag{B5}$$

$$g_2 = 2T^* \sum_{m=1}^{\infty} \left\{ \frac{\{\exp[-\lambda_m(t^* + \theta_1 + \theta_3)] - \exp[-\lambda_m(t^* + \theta_1 + \theta_3 + \theta_2)]\}}{\lambda_m} \times \left\{ \frac{1 - \exp[-\lambda_m(p-1)]}{1 - \exp[-\lambda_m]} \right\} \right\} \tag{B6}$$

$$g_3 = 2T^* \sum_{m=1}^{\infty} \left\{ \frac{\{\exp[-\lambda_m(t^* + \theta_1)] - \exp[-\lambda_m(t^* + \theta_1 + \theta_3)]\}}{\lambda_m} \times \left\{ \frac{1 - \exp[-\lambda_m(p-1)]}{1 - \exp[-\lambda_m]} \right\} \right\} \tag{B7}$$

$$G_2 = g_1 + g_2 + g_3 = 2T^* \sum_{m=1}^{\infty} \left\{ \frac{\{\exp[-\lambda_m t^*]\}}{\lambda_m} \times \{1 - \exp[-\lambda_m(p-1)]\} \right\}$$
$$+ 2T^* \sum_{m=1}^{\infty} \left\{ \frac{\{\exp[-\lambda_m t^*] - \exp[-\lambda_m(t^* + \theta_1)]\}}{\lambda_m} \times \{\exp[-\lambda_m(p-1)]\} \right\} \tag{B8}$$

(*iii*) *Anodic duty cycle* $(0 < t^* < \theta_3)$

$$g_1 = 2T^* \sum_{m=1}^{\infty} \left\{ \frac{\{\exp[-\lambda_m(t^* + \theta_2)] - \exp[-\lambda_m(t^* + \theta_2 + \theta_1)]\}}{\lambda_m} \times \left\{ \frac{1 - \exp[-\lambda_m p]}{1 - \exp[-\lambda_m]} \right\} \right\} \tag{B9}$$

$$g_2 = 2T^* \sum_{m=1}^{\infty} \left\{ \frac{\{\exp[-\lambda_m t^*] - \exp[-\lambda_m(t^* + \theta_2)]\}}{\lambda_m} \times \left\{ \frac{1 - \exp[-\lambda_m p]}{1 - \exp[-\lambda_m]} \right\} \right\} \tag{B10}$$

$$g_3 = 2T^* \sum_{m=1}^{\infty} \left\{ \frac{\{\exp[-\lambda_m(t^* + \theta_1 + \theta_2)] - \exp[-\lambda_m(t^* + \theta_1 + \theta_2 + \theta_3)]\}}{\lambda_m} \times \left\{ \frac{1 - \exp[-\lambda_m(p-1)]}{1 - \exp[-\lambda_m]} \right\} \right\} \tag{B11}$$

$$G_3 = g_1 + g_2 + g_3 = 2T^* \sum_{m=1}^{\infty} \left\{ \frac{\{\exp[-\lambda_m t^*]\}}{\lambda_m} \times \{1 - \exp[-\lambda_m p]\} \right\}$$
$$+ 2T^* \sum_{m=1}^{\infty} \left\{ \frac{\{\exp[-\lambda_m(t^* + \theta_1 + \theta_2)] - \exp[-\lambda_m(t^* + \theta_1 + \theta_2 + \theta_3)]\}}{\lambda_m} \times \{\exp[-\lambda_m p]\} \right\} \tag{B12}$$

(*iv*) *Common functions*

$$s = 2T^* \sum_{m=1}^{\infty} \frac{1}{\lambda_m} \tag{B13}$$

$$r = 2T^* \sum_{m=1}^{\infty} \left\{ \frac{\exp[-\lambda_m t^*]}{\lambda_m} \right\} \tag{B14}$$

$$\lambda_m = \pi^2 T^* (m - 0.5)^2 \qquad \text{for } m = 1, 2, 3, \ldots, \infty \tag{B15}$$

Appendix C: Definition of functions for Equations 29–31

(*i*) *For any period p*

$$f_{1,p} = 2T^* \sum_{m=1}^{\infty} \left\{ \frac{1}{\lambda_m} \times \{1 - \exp[-\lambda_m \theta_1]\} \times \left\{ \frac{1 - \exp[-\lambda_m p]}{1 - \exp[-\lambda_m]} \right\} \right\} \tag{C1}$$

$$f_{2,p} = 2T^* \sum_{m=1}^{\infty} \left\{ \frac{1}{\lambda_m} \times \{\exp(-\lambda_m[1-\theta_2]) - \exp[-\lambda_m]\} \times \left\{ \frac{1-\exp[-\lambda_m(p-1)]}{1-\exp[-\lambda_m]} \right\} \right\} \tag{C2}$$

$$f_{3,p} = 2T^* \sum_{m=1}^{\infty} \left\{ \frac{1}{\lambda_m} \times \{\exp[-\lambda_m\theta_1] - \exp[-\lambda_m(1-\theta_2)]\} \times \left\{ \frac{1-\exp[-\lambda_m(p-1)]}{1-\exp[-\lambda_m]} \right\} \right\} \tag{C3}$$

$$\mathscr{F} = f_{1,p} + f_{2,p} + f_{3,p} = 2T^* \sum_{m=1}^{\infty} \left\{ \frac{1}{\lambda_m} \times (1 - \exp[-\lambda_m(p-1+\theta_1)]) \right\} \tag{C4}$$

(ii) For infinite times $(p \to \infty)$

$$f_{1,\infty} = 2T^* \sum_{m=1}^{\infty} \frac{1-\exp[-\lambda_m\theta_1]}{\lambda_m\{1-\exp[-\lambda_m]\}} \tag{C5}$$

$$f_{2,\infty} = 2T^* \sum_{m=1}^{\infty} \frac{\exp[-\lambda_m(1-\theta_2)] - \exp[-\lambda_m]}{\lambda_m\{1-\exp[-\lambda_m]\}} \tag{C6}$$

$$f_{3,\infty} = 2T^* \sum_{m=1}^{\infty} \frac{\exp[-\lambda_m\theta_1] - \exp[-\lambda_m(1-\theta_2)]}{\lambda_m\{1-\exp[-\lambda_m]\}} \tag{C7}^{\dagger}$$

where

$$\lambda_m = \pi^2 T^* (m-0.5)^2 \qquad \text{for } m = 1, 2, 3, \ldots \infty \tag{C8}$$

† The error in this equation (Equation 27(a) in ref. [31]) was previously detected by us and recently corrected by Wang *et al.* [52].